Chapter – 3

Composition modulation, strain minimization and oriented growth of phases in equimolar (CaCoFeMgNi) multicomponent oxide

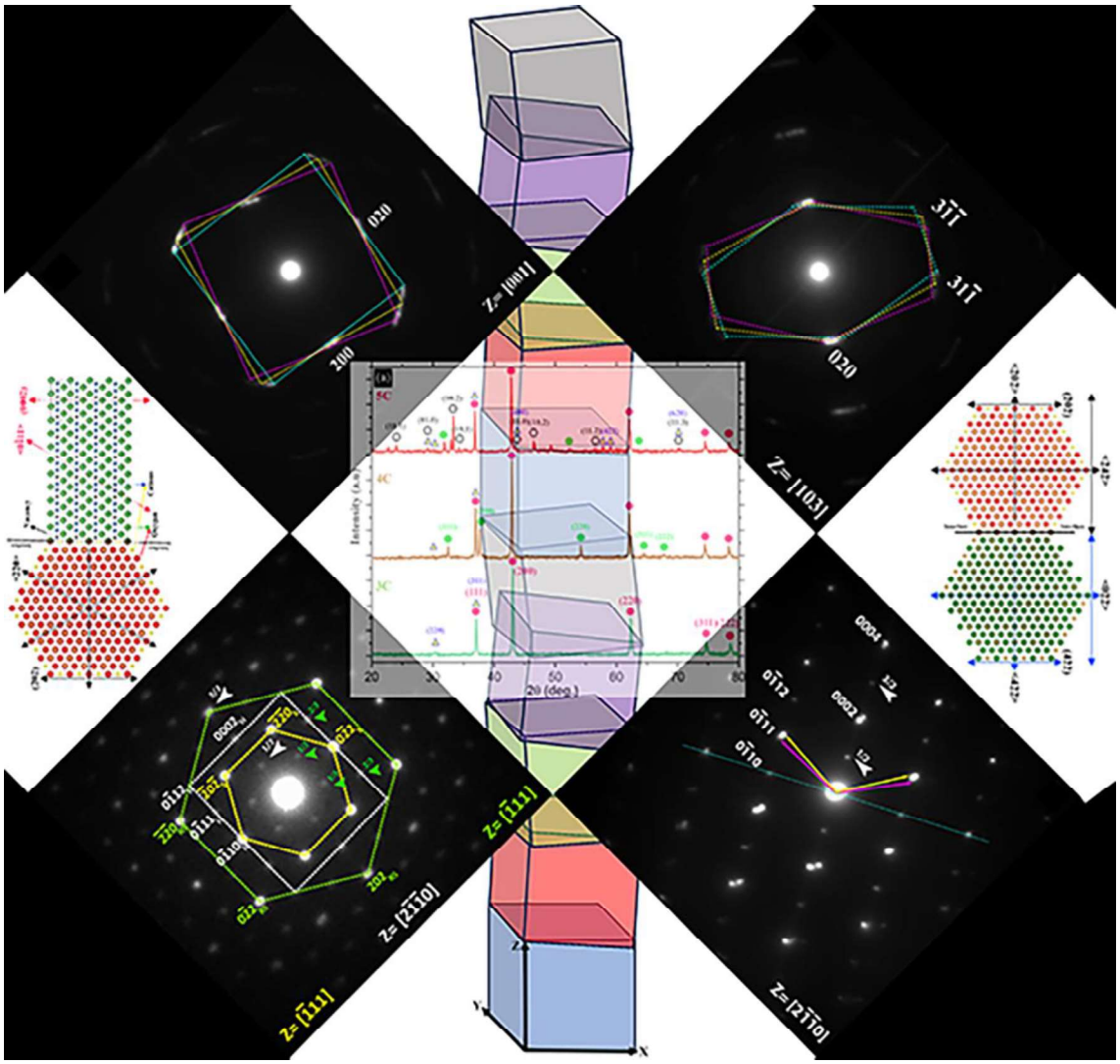

3.1. Introduction

Continuously depleting fossil fuel resources, growing environmental concerns, changing geopolitical scenario and ever-increasing energy needs have incentivized in simulating a fresh search on economically sustainable, environmentally friendly, robust energy harvesting and storage technologies [1-2]. While the operational mechanisms of fundamental principles for energy harvesting and storage are being researched at atomic and nanometer length scales, search for advanced materials, which can provide a suitable platform for efficient exploitation of the fundamental principles at atomic and nanometer length scales has also become an important facet globally [3-5]. High entropy materials (HEMs), especially high entropy ceramics (HECs) has received a lot of attention in the recent past as it is envisaged as a potential candidate material for energy harvesting and storage pertaining to its favorable electrochemical, thermoelectric and catalytic properties [6-8].

Over the last two decades, a considerably good volume of data on design, microstructure evolution, phase stability and properties on high entropy alloys (HEAs) have been documented in scientific literature [9-11]. In comparison to that, high entropy oxides (HEOs) or high entropy ceramics (HECs) are of recent vintage. The scientific literature on these materials is not so much enriched so far, their design principles, microstructure evolution, phase stability and properties are concerned [12]. HEOs/HECs may be considered to be developed in the natural evolutionary process of HEAs [6, 13]. However, there are certain fundamental concepts, e. g. assessment of configurational entropy, that need to be treated differently as the HEOs/HECs are ionic in nature and there are separate sublattices for cations and anions [14]. Initially it was believed that for HEAs with more than or equal to five elements, the configurational entropy was so high that the entropy term always dominated the total free energy of the system [15]. However, of late it is observed

that many of the HEAs are metastable in nature, more than two phases form in the traditional HEAs, which has put a question mark in front of the high configurational entropy concept extended so far in order to explain their microstructure evolution and phase stability [9, 16-17]. It is now proposed that HEA is a misnomer [18] and this kind of alloys should be termed as multi-principal element alloys (MPEAs) or complex concentrated alloys (CCAs) [19-20]. HEOs/HECs are also believed to be entropy stabilized single phase solid solutions. The role of strain energy in the lattice of HEOs/HECs, due to the presence of ions of different sizes, in determining its microstructure evolution and phase stability has remained almost unexplored [21-22].

It is believed that in HEOs, isostructuralism of precursor oxide components that finally builds up the HEO would always favor single phase HEO formation. It may accommodate one or two non-isostructural oxide components. In addition to that negative enthalpy of mixing and low to moderate difference in ionic sizes will favor the formation of single-phase HEOs [14, 23]. The work has been taken up to test the significance of the postulates and to explore the role of strain energy arising out of ionic radii and interface incoherency in a quinary equimolar (CaCoFeMgNi)-oxide. The phase stability and microstructure evolution has been compared with the ternary (CoMgNi)-oxide and quaternary (CaCoMgNi)-oxide derivatives of the original quinary equimolar (CaCoFeMgNi)-oxide. The precursor oxides of the multicomponent quinary oxide are the oxides of Ca, Co, Fe, Mg and Ni, all of which are cubic rocksalt in structure in the +2-oxidation state of the respective cations. The cation sublattice of the quinary multicomponent HEO is likely to be substituted by the ions of Ca, Co, Mg, Fe and Ni. The ionic radii of Co, Mg, Fe and Ni are close to one another. However, the ionic radius of Ca is different from the other cations [24-25] in the same coordination environment. In this work, the role of micro-strain in the lattice induced by different cations and the strain induced by interface incoherency have

been investigated. Finally, it has been established that the quinary oxide is not solely configurational entropy stabilized. However, it's a trade-off between the strain energy and the entropy that eventually determines the phase stability and microstructure evolution in this multicomponent oxide.

3.2. Materials and methods

Phase evolution, composition modulation and oriented structural intergrowth has been studied in equimolar CaCoFeMgNi multicomponent oxide. High purity metal oxide; CaO (>99.95 at%), Co(II, III)O (>99.8 at%), Fe (II, III)O (>99.8 at%), MgO (99.98 at%) and NiO (99.9 at%) were procured from either Sigma Aldrich or Alfa Aesar. Oxides in equimolar proportions were mixed together and were thoroughly ground in a mortar and pestle before they were green compacted in a uniaxial hydraulic press with 4 Ton load. In one set of samples, the mixed metal oxides in equimolar proportions were ball milled for 40 h in dry environment in a zirconia vial with zirconia balls with ball to powder ratio 10:1 before it was green compacted in a uniaxial hydraulic press with 4 Ton load. Green compacted mixed oxide pellets of 12 mm diameter were sintered at 1523 K (1250 ^{o}C) for 10, 25 and 100 h in air atmosphere and the sintered pellets were quenched in water. The sintering was carried out in a platinum crucible with the platinum lid on. Three green compacted pellets of similar composition were vertically stacked in the platinum crucible and the sintered pellet from the center of the stack was taken for further studies in order to avoid contamination during sintering. Sintered pellets were ground and polished from both sides and were studied by a Malvern Panalytical Empyrean high-resolution x-ray diffractometer with Cu-K_{α} radiation operated at 40 kV operating voltage with 40 mA current. Relative volume fraction of the phases was determined by peak ratio method of the x-ray diffraction (XRD) peaks. Microstructure and composition of the sintered pellets were studied in a FEI Quanta 200F scanning electron microscope (SEM) with an accelerating

voltage of 30 kV. For SEM studies the sintered and quenched pellets were metallographically polished and ultrasonicated in ethanol. X-ray energy dispersive spectroscopy (XEDS) mapping of the samples was done at the regions of interest in order to understand the distribution of the ions. The sintered and quenched pellets were studied in a FEI Tecnai G2 T20 transmission electron microscope (TEM) under 200 kV accelerating voltage. For TEM observations, the sintered and quenched samples were sliced by a low-speed saw, ground and polished to optimal thickness and it was ion-beam thinned to electron transparency.

The simulation of x-ray diffraction patterns was done by indigenously developed code and JEMS software was used for simulation of electron diffraction patterns. VESTA^{TM} software was used for development of crystal structure models.

3.3. Results

Phase evolution in equimolar ternary (CoMgNi)-oxide, quaternary (CaCoMgNi)-oxide and quinary (CaCoFeMgNi)-oxide after sintering at 1523 K for 10 h and water quenching has been studied through powder x-ray diffraction. The experimental powder x-ray diffraction pattern from the equimolar sintered and quenched ternary (CoMgNi)-oxide is given in Figure 3.1a-3C. The diffraction peaks are quite sharp with minimal broadening and all of them match with the solid solution phase of CoO, MgO and NiO with cF8 rocksalt structure with ~4.21 Å lattice parameter. There are two peaks, which could be indexed to cF56 (Ni,Mg)Co_2O_4 spinel phase with ~8.41 Å lattice parameter. However, the presence of this phase cannot be confirmed at this stage. Even if it is assumed to be present, its volume fraction is supposed to be very small. The simulated x-ray diffraction pattern corresponding to the CoO, MgO and NiO based solid solution phase with cF8 rocksalt structure (Figure 3.1b, in red) matched quite accurately with the experimental x-ray diffraction pattern.

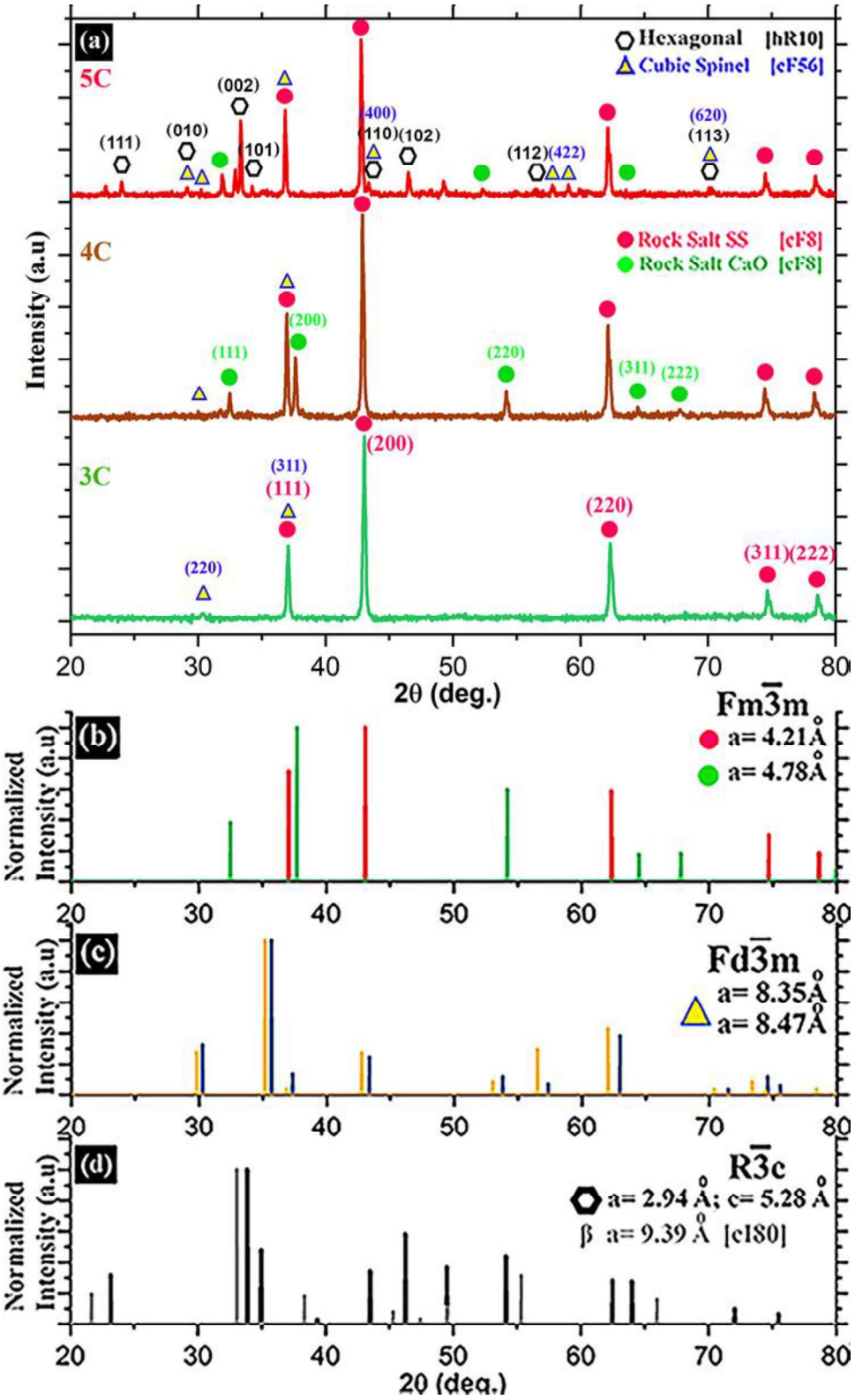

Figure 3.1: Experimentally observed x-ray powder diffraction pattern of (a-3C) ternary (CoMgNi)-oxide (a-4C) quaternary (CaCoMgNi)-oxide (a-5C) quinary (CaCoFeMgNi)-oxide after sintering at 1523 K for 10 h followed by water quenching. Simulated X-ray powder diffraction pattern of (b) cubic rocksalt structure with ~4.21 Å and ~4.78 Å lattice parameters (c) cubic spinel structure with ~8.35 Å and ~8.47 Å lattice parameters and (d) hexagonal phase with a ~2.94 Å, c ~5.28 Å lattice parameter and cubic Fe_2O_3 with ~9.39 Å lattice parameter.

The sharpness of the experimental diffraction peaks indicates that the solid solution phase does not have quenching or solid solutioning induced residual strain in it. However, weak shouldering is observed in the 200, 220, 311 and 222 peaks, which might indicate a possibility of polymorphic transformation of the cubic rocksalt phase to a tetragonal phase. However, it cannot be confirmed at this stage and it would require further investigation. Additional diffraction peaks are observed in the experimental x-ray diffraction pattern from the sintered and quenched equimolar quaternary (CaCoMgNi)-oxide sample (Figure 3.1a-4C). In addition to the solid solution phase of (CoMgNi)-oxide with cubic rocksalt structure with ~4.21 Å lattice parameter, another isostructural solid solution phase based on CaO with ~4.78 Å lattice parameter is observed. The relative volume fractions are ~61.2% and ~38.8% for the (CoMgNi)-oxide and CaO-based oxide SS phases respectively. In this diffraction pattern, the peaks are quite sharp with minimal broadening indicating minimal or almost no solid solutioning or quenching induced residual strain in the sample. However, the shoulders in the diffraction peaks corresponding to the (CoMgNi)-oxide are still observed. The shouldering in the CaO based solid solution phase is also present. However, not so prominent at lower diffraction angles. The simulated polycrystalline x-ray diffraction pattern for the CaO based solid solution phase with rocksalt structure (Figure 3.1b, in green) match quite well with the experimental pattern. It may be concluded from these observations that a solid solution phase with cubic rocksalt structure forms in the equimolar (CoMgNi)-oxide upon sintering at 1523 K for 10 h followed by quenching. However, upon addition of CaO, two isostructural solid solution phases with rocksalt structure and with different lattice parameters are observed. The reason behind such observation would be discussed in the discussion section.

Quite a few additional diffraction peaks are observed in the experimental x-ray diffraction pattern of the equimolar quinary (CaCoFeMgNi)-oxide after sintering at 1523 K for 10 h

followed by quenching (Figure 3.1a-5C). In this diffraction pattern, in addition to the solid solution phases based on (CoMgNi)-oxide with ~4.21 Å lattice parameter, CaO based solid solution phase with ~4.78 Å lattice parameter, a spinel phase with ~8.41 Å lattice parameter is also present. The spinel phase brings out a very good match with the simulated polycrystalline diffraction pattern (Figure 3.1c) of $(Ni,Fe)Co_2O_4$ spinel (in blue) with ~8.35 Å lattice parameter and $(Ca,Fe)_3O_4$ spinel (in yellow) with ~8.47 Å lattice parameter. It is assumed that the experimentally observed spinel phase is a chemical and structural derivative of the two above mentioned spinel phases. In addition to that, a hexagonal phase (hR10) with quite similar symmetry elements to that of Fe_2O_3 is observed. The simulated diffraction pattern of the hexagonal phase (Figure 3.1d) with lattice parameter a ~2.94 Å and c ~5.28 Å matches closely with the experimental diffraction peaks of the hexagonal phase in Figure 3.1a-5C. It is assumed that the hexagonal phase is a derivative of Fe_2O_3 phase. The structural details of this phase will be presented later in this paper through electron diffraction. The relative volume fraction of (CoMgNi)-oxide based SS phase, CaO-based SS phase, spinel phase and the hexagonal phase are ~48.1%, ~11.25%, ~5.12% and ~35.5% respectively. It is important to point out that there is a cubic polymorph (cI80) of Fe_2O_3 phase, the simulated diffraction pattern of which is given in Figure 3.1d (in grey). However, it shows a weak match with the experimental diffraction pattern (Figure 3.1a-5C). It is assumed that the cubic polymorph is not present in the sintered and quenched (CaCoFeMgNi)-oxide. It is observed that multiple phases are formed in the quinary (CaCoFeMgNi)-oxide after sintering at 1523 K for 10 h followed by water quenching. In order to explore the effect of processing route, the as-mixed quinary oxide was ball milled for 40 h and then the milled green compact was sintered at 1523 K for 10 h followed by water quenching.

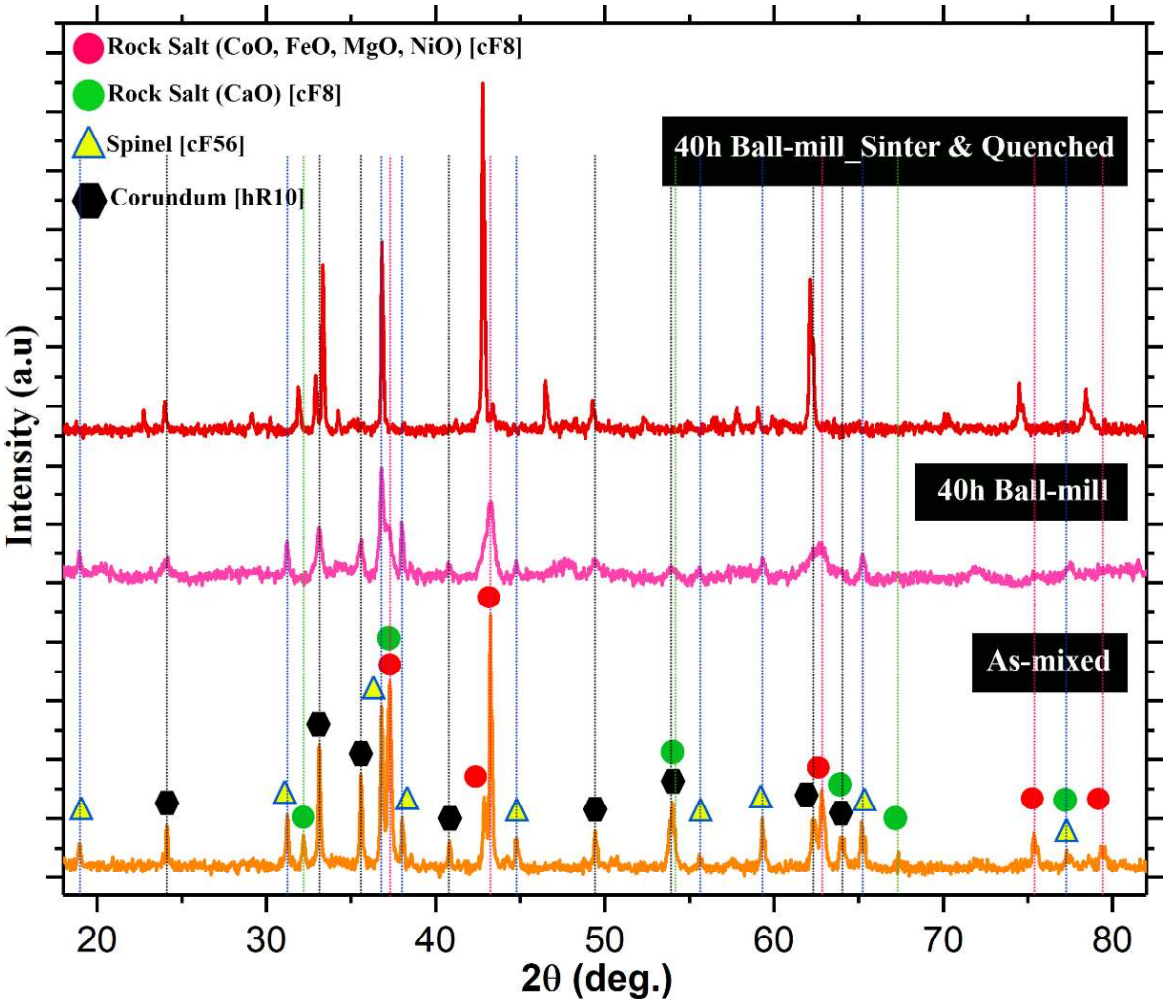

Figure 3.2: Experimentally observed powder x-ray diffraction patterns of as-mixed (CaCoFeMgNi) precursor oxide powders in equimolar ratio (in orange), the same as-mixed powder after dry ball milling for 40 h (in pink) and the pellet after sintering the green compacted ball milled powder at 1523 K for 10 h followed by water quenching (in red). In the sintered pellet cubic rocksalt phase, cubic spinel phase and the hexagonal phase can be indexed.

In the powder x-ray diffraction pattern of the as mixed quinary oxide (Figure 3.2, in orange) all the diffraction peaks corresponding to CaO, CoO, FeO, MgO, NiO, Co_3O_4 / Fe_3O_4 spinel and Fe_2O_3 corundum phases are present. After 40 h of ball milling the diffraction peaks are broadened (Figure 3.2, in pink) with a drop in intensity. The individual oxide phases cannot be distinguished anymore with certainty. This observation may be explained in the light of accumulation of strain and minor solid solutioning of oxide phases during ball milling. However, the as-mixed, ball milled and green compacted pellet after sintering at 1523 K

for 10 h followed by water quenching gives rise to a diffraction pattern (Figure 3.2, in red), which is quite similar to the as-mixed, green compacted, sintered at 1523 K for 10 h and quenched diffraction pattern of the same quinary oxide (Figure 3.1a-5C). It may be easily concluded from this observation that intermediate ball milling does not have any significant influence in the phase evolution in this quinary oxide.

In order to understand the phase and microstructural stability, green compacted equimolar (CaCoFeMgNi)-oxide was sintered at 1523 K for different length of time i. e. for 10, 25, 100 h followed by water quenching.

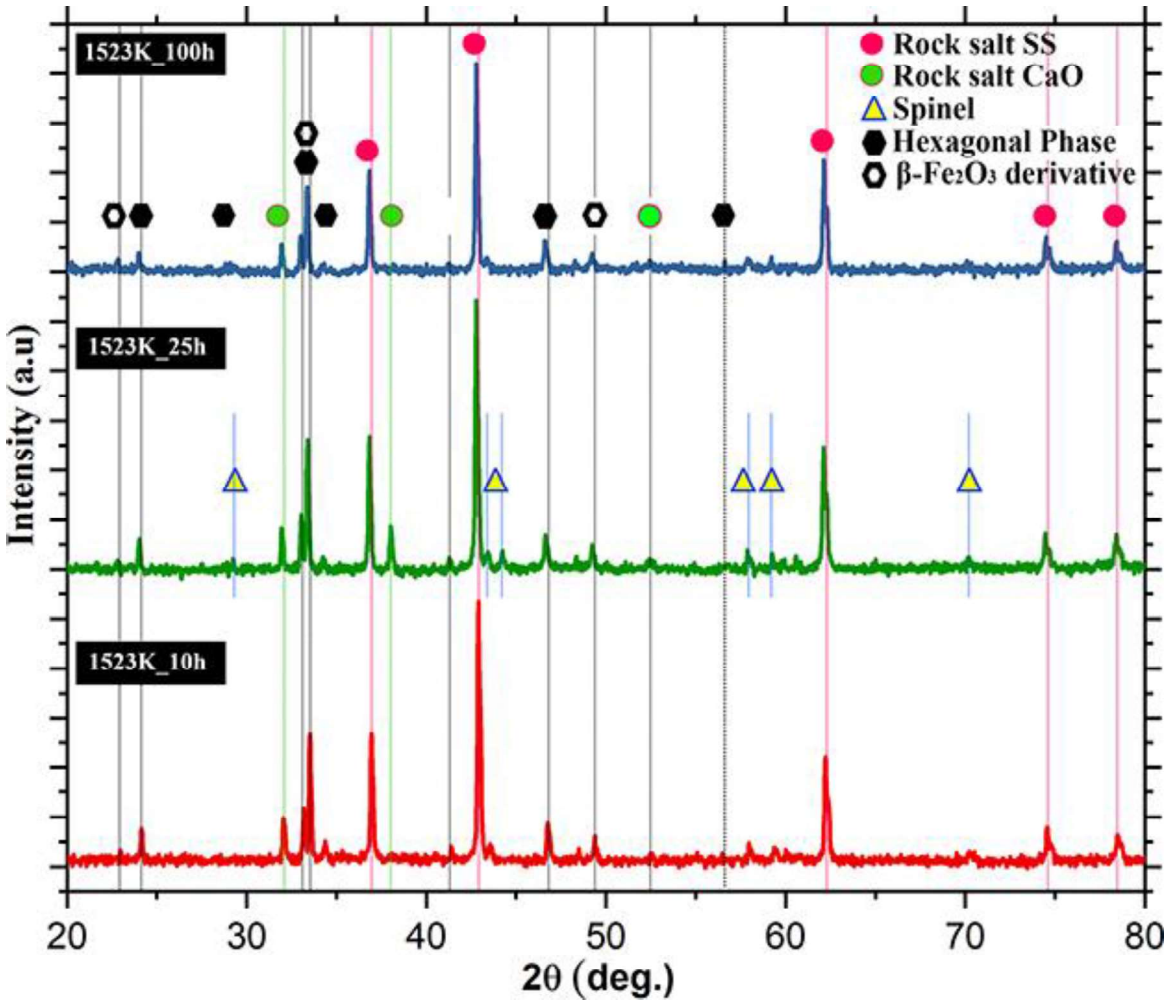

Figure 3.3: Experimentally observed x-ray diffraction patterns of quinary equimolar (CaCoFeMgNi)-oxide pellet after sintering at 1523 K for 10 h (in red), 25 h (in green) and 100 h (in blue). In all the sintered pellets cubic rocksalt phase, cubic spinel phase and the hexagonal phase can be indexed.

The multiple display of x-ray diffraction patterns after sintering for different length of time followed by water quenching is given in Figure 3.3. It is observed that cubic solid solution phase with rocksalt structure, however, based on CaO and (CoMgNi)-O with ~4.78 Å and ~4.21 Å lattice parameters respectively are still present in all of 10 h, 25 h and 100 h sintered samples. The hexagonal phase with a ~2.94 Å and c ~5.28 Å lattice parameter, which is considered to be a chemical and structural derivative of hexagonal Fe_2O_3 is present in all the three sintered samples. The cubic spinel phase with ~8.41 Å lattice parameter, which is assumed to be the chemical derivative of (Ni,Fe)Co_2O_4 (a = 8.35 Å) and $(Ca,Fe)_3O_4$ (a = 8.47 Å) is also present in all three sintered samples. However, the signature of the spinel phase is most prominent in the 25 h sintered sample. It may be concluded from this observation that the phases are stable up to 100 h of sintering time. Only the spinel phase becomes most prominent in the 25 h sintered samples and it is not so prominent in the 10 h and 100 h sintered samples. The solid-solution based spinel phase obtained in the present study may be seen to be structurally related with the solid-solution based rocksalt phases in terms of octahedral void filling. The probable structural correlation will be discussed in the discussion section in detail, which will explain the prominent presence and partial disappearance of the spinel phase.

SEM secondary electron micrograph of quinary equimolar (CaCoFeMgNi)-oxide sintered at 1523 K for 10 h followed by water quenching (Figure 3.4A) and its zoomed-in version (Figure 3.4a) shows irregular grain structure in the size range of ~ 5-10 μm. Pores are not observed significantly in the microstructure. The XEDS chemical mapping from the zoomed-in area (Figure 3.4a) clearly indicates chemical segregation during the sintering process. As seen from the maps, Fe and Ca ions get segregated in the grains and the boundary regions are enriched with Co, Mg and Ni ions.

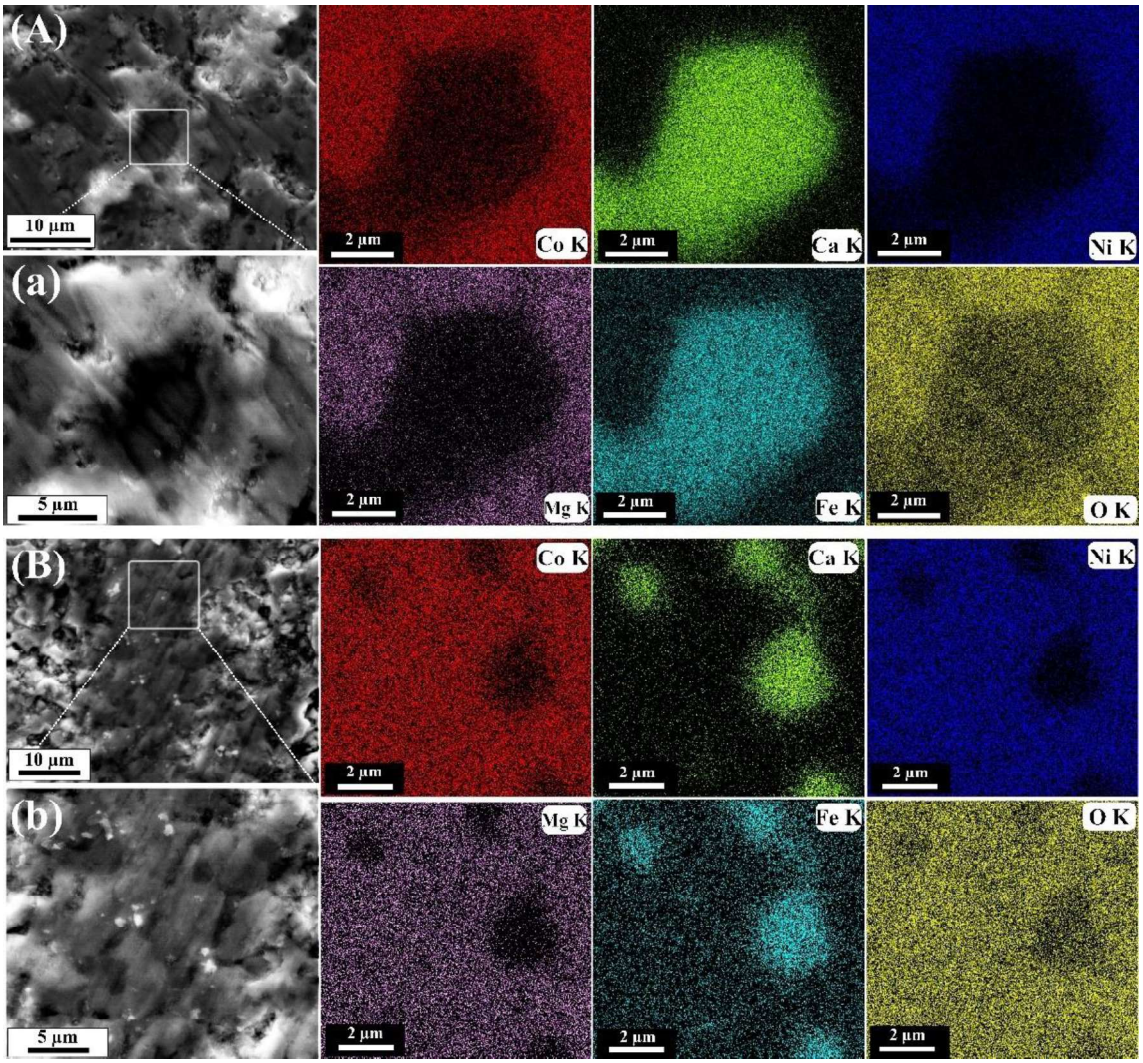

Figure 3.4: SEM-XEDS area map with Ca-K, Co-K, Fe-K, Mg-K and Ni-K in quinary equimolar (CaCoFeMgNi)-oxide after (A) sintering at 1523 K for 10 h and (B) sintering at 1523 K for 100 h followed by water quenching. (a) is the zoomed-in version of the area marked in (A) and (b) in the zoomed-in version of the area marked in (B). The XEDS maps are generated from the areas shown in (a) and in (b). In both the samples, two chemically segregated regions, one rich in Co, Mg, Ni ions and other rich in Ca and Fe ions can be observed.

This observation further reinforces the analytical outcomes of the XRD patterns in Figures 3.1, 3.2 and 3.3, where solid solution phases based on (CoMgNi)-oxide and CaO has been reported. Further, the spinel phase is reported to be a chemical derivative of $(Ni,Fe)Co_2O_4$ and $(Ca,Fe)_3O_4$. It is highly likely that the spinel phase may exist in both the regions. The hexagonal phase, which is assumed to be a chemical derivative of hexagonal Fe_2O_3 is likely to be present in the Ca and Fe enriched areas. It may be concluded that CaO based solid

solution phase, the spinel phase and the hexagonal phase coexist in the Ca and Fe enriched regions, whereas the (CoMgNi)-O based solid solution phase and the spinel coexist in the Co, Mg, Ni enriched regions. Their coexistence behaviour will be reported in the subsequent sections. It is noteworthy at this point that oxygen mapping reveals qualitatively non-uniform distribution of oxygen. It is preferentially enriched in the areas where solid solution phase based on (CoMgNi)-oxide and the spinel phase are present. It is depleted in the regions where CaO based solid solution phase, spinel phase and the hexagonal phase coexist. SEM secondary electron image (Figure 3.4B) and its zoomed-in version (Figure 3.4b) indicates that after 100 h of sintering followed by water quenching there is no significant change in the microstructure. The grains are still irregular in shape with insignificant or almost no grain growth during the elongated sintering process. After 100 h of sintering the grain size is ~ 5-15 μm. In this sample also the porosity remains to be very low. XEDS chemical maps from the zoomed-in area in Figure 3.4b indicates segregation of Ca and Fe with respect to Co, Mg and Ni. Inhomogeneous distribution of oxygen and its preferential segregation in the Co, Mg, Ni enriched regions are also noteworthy. The XEDS chemical map from Figure 4b shows chemical segregation in multiple pockets, which further reinforces the claim that the chemical segregation is characteristic of the sintered microstructure.

SEM-BSE image of sintered and quenched (CaCoFeMgNi)-oxide (1523K, 10h) along with point XEDS spectra and relative composition of the phases from several regions are given in Figure 3.5. The variation in contrast arising out of chemical segregation is clearly evident from the BSE image. Additionally, point EDS has been carried out on regions of interest. Six such regions have been chosen of varying contrast and they have been categorized and clubbed in the table below (Figure 3.5). It is seen that the pair of regions marked as 1,6 have similar chemical distribution while the pair marked as 2,3 in turn have similar

chemical distribution, however different from each other. Similarly, regions marked as 4 and 5 are compositionally different from each other as well as from region pairs 1,6 and 2,3. The relative volume fraction listed in the last column of the table has been deduced from curve profile fitting of the XRD patterns reported in Figures 3.1-3.3, and its subsequent calibration through peak intensity ratio method. It may therefore be concluded from point EDS analysis that in the Co, Mg, Ni rich regions Ca and Fe ions are present in minor quantities and vice-versa, which further reinforces inference drawn from Figure 3.4.

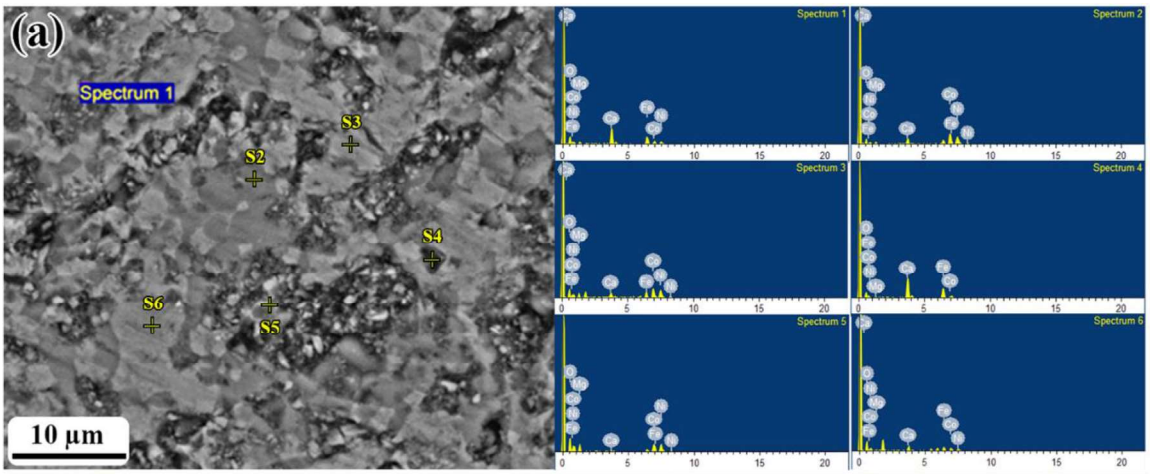

S1	Wt. %	S2	Wt. %	S3	Wt. %	S4	Wt. %	S5	Wt. %	S6	Wt. %
Ca	25.43	Ca	5.52	Ca	4.59	Ca	26.86	Ca	0.38	Ca	17.41
Co	11.7	Co	36.71	Co	29.54	Co	5.25	Co	27.4	Co	10.05
Fe	18.96	Fe	9.59	Fe	11.43	Fe	37.61	Fe	4.92	Fe	15.6
Mg	3.52	Mg	4.06	Mg	6.64	Mg	0.12	Mg	12.33	Mg	3.56
Ni	9.55	Ni	30.94	Ni	30.85	Ni	1.85	Ni	28.1	Ni	13.14

	Chemical distribution	Phase (P)	P. Fraction
Region 1,6	*Rich in Ca, Fe ; Moderate in Co, Ni ; Lean in Mg*	*Cubic Rock salt (a= 4.83 Å)*	~ 11.2%
Region 2,3	*Rich in Co, Ni ; Moderate in Fe, Mg ; Lean in Ca*	*Cubic Spinel (a= 8.32 Å)*	~ 5.1%
Region 4	*Rich in Fe, Ca ; Moderate in Co ; Lean in Mg, Ni*	*Ordered Hexagonal (a=2.94 Å, c=5.28 Å)*	~ 35.5%
Region 5	*Rich in Co, Mg, Ni ; Lean in Ca, Fe (major phase)*	*Cubic Rock salt (a= 4.15 Å)*	~ 48.1%

Figure 3.5: (a) Back scattered electron (BSE) image and X-ray energy dispersive spectrum (XEDS) from the points marked by s1-s6 in (CaCoFeMgNi)-oxide sintered at 1523K for 10h. Compositional contrast is observed in the BSE image. All the point XEDS from s1-s6 show the presence of all the elements, however in varying quantities. Compositions as obtained from XEDS are tabulated in the table below. It is again reconfirmed that Ca and Fe ion rich regions are relatively lean in Co, Mg and Ni ions and vice-versa. However, all the elements are present in all the phases. Based on the composition the predominant phase in different regions have been identified and their volume fraction as computed from the X-ray diffraction peak analysis is given in the table at the bottom of the figure.

TEM bright field images and corresponding electron diffraction patterns for quinary equimolar (CaCoFeMgNi)-oxide after sintering at 1523 K for 10 h followed by water quenching are given in Figure 3.6 (a-d). After sintering for 10 h followed by quenching, polygonal and faceted (Figure 3.6a) grains can be observed in the microstructure. Thickness fringes within the grains indicates that the grains are polyhedral in shape. The corresponding diffraction pattern in Figure 3.6b is a z = [001] zone axis pattern of a cubic phase. The 200 and 220 plane spacings as measured from this diffraction pattern turns out to be ~2.06 Å and ~1.45 Å respectively, which are very close to the same d-spacings of the (CoMgNi)-oxide solid solution phase as obtained from the x-ray diffraction pattern. The calculated lattice parameter for this solid solution phase turns out to be ~4.16 Å, which is within ~2% error range of calculated lattice parameter of the same phase as obtained from the x-ray diffraction pattern. Bright field image from the same 10 h sintered and quenched sample but from a different region is given in Figure 3.6c. In this image also faceted grain is observed. However, within the grain considerable amount of mottled contrast is present, which indicates the presence of micro-strain within the grain body. The corresponding diffraction pattern (Figure 3.6d) is along cubic z = [103] zone axis, which matches with the same cubic solid solution phase of (CoMgNi)-oxide with rocksalt structure with ~4.16 Å lattice parameter. Bright field images from two different regions after sintering at 1523 K for 100 h followed by water quenching are given in Figure 3.6e and Figure 3.6g respectively. In both the images the grains are quite large. However, within the grains strong mottled contrast is observed. A careful look reveals a fringe contrast (pointed with black arrows) within the mottled regions. The origin of the fringe contrast within the mottled regions is not directly interpretable from the images. However, the corresponding diffraction patterns from the respective regions (Figure 3.6f and Figure 3.6h) offer interesting insights about accumulated micro-strain in the lattice, which might be treated as

the origin of fringe contrast in the bright field images and the tendency of the system to minimize it in the process of long-term sintering. The diffraction pattern in Figure 3.6f corresponds to the region in the bright field image in Figure 3.6e. In the diffraction pattern cubic 4-fold symmetry is quite easily discerned. However, the principal reflections are arced instead of being spots with several intensity maxima present in each of them. When the intensity maxima present in each of the arcs are joined geometrically by dotted coloured lines as has been done in Figure 3.6f, presence of several square patterns rotated with respect to one another by a very small angle is observed. However, in this image only three such square patterns are shown for the purpose of clarity.

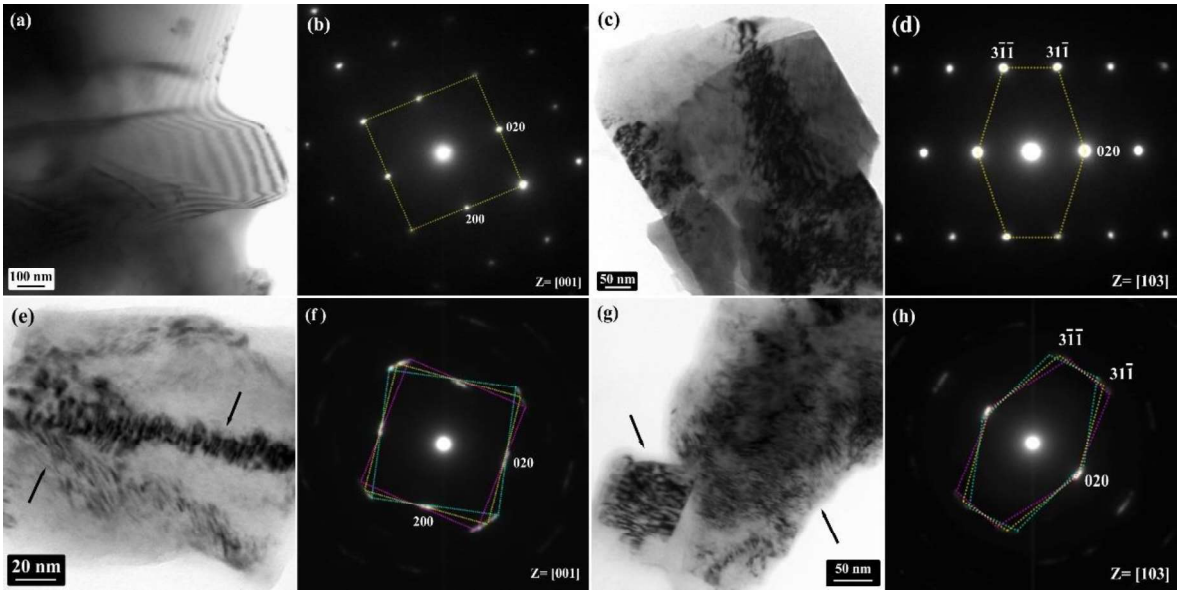

Figure 3.6: TEM (a, c) BF images and corresponding (b, d) single crystal diffraction patterns from z = [001] and z = [103] respectively in quinary equimolar (CaCoFeMgNi)-oxide after sintering at 1523 K for 10 h followed by water quenching. Thickness fringes in (a) and mottled contrast in (b) can be observed. The diffraction patterns in (b) and (d) are sharply defined. TEM (e, g) BF images and corresponding (f, h) single crystal diffraction patterns from z = [001] and z = [103] respectively in quinary equimolar (CaCoFeMgNi)-oxide after sintering at 1523 K for 100 h followed by water quenching. In the BF images in (e) and (g) fringe contrast within the mottled regions (marked with arrows) can be observed. In the diffraction patterns in (f) and in (h) arcs with modulated intensities can be observed.

The diffraction pattern (Figure 3.6h) from the region given in the bright field image in Figure 3.6g also shows similar arcing with several intensity maxima. In this diffraction pattern, when the intensity maxima are geometrically connected by dotted lines, each of the dotted polygons in the shape of distorted hexagons conforms to the z = [103] zone axis pattern of a cubic phase, which matches quite closely with the solid solution phase of (CoMgNi)-oxide with rocksalt structure with ~4.16 Å lattice parameter. In Figure 3.6h three such dotted coloured polygons are shown for the purpose of clarity. The presence of arcs in the diffraction patterns after 100 h of sintering (Figure 3.6f and Figure 3.6h) and simultaneous presence of fringe contrast in the mottled regions in the bright field images (Figure 3.6e and Figure 3.6g) confirms that the (CoMgNi)-oxide solid solution phase with rocksalt structure is rotated with respect to one another successively through a very small angle. The diffraction pattern in Figure 3.6f is along z = [001] and the intensity along any arc is not totally uniform. This indicates that the solid solution phase with rocksalt structure has a successive in-plane small angle rotation when viewed along z= [001]. However, non-uniform intensity distribution indicates to the probability of having an out-of-plane rotation between two successive cubic domains, which can be confirmed from the diffraction pattern in Figure 3.6h with viewing direction as z = [103]. Along this zone axis also, arcing and non-uniform intensity distribution is observed, which necessarily indicates the successive rotation between the cubic domains resulting into an inter-penetration between two consecutive domains in 3-dimension. As the zone axes in Figure 3.6f (z = [001]) and Figure 3.6h (z =[103]) are not mutually perpendicular to one another, arcing in both the diffraction patterns may be treated as the confirmatory evidence of interpenetration of mutually rotated cubic domains in 3-dimension. The detailed structural model and possible mechanism behind the formation of such inter-penetrated domains will be discussed in the discussion section.

Selected area diffraction pattern from another region of the quinary equimolar (CaCoFeMgNi)-oxide after sintering at 1523 K for 10 h and 100 h followed by water quenching is given in Figure 3.7a and Figure 3.7b respectively. In both the diffraction patterns multiple spots with modulation of intensity could be observed. The measured d-spacings from the diffraction pattern are marked in Figure 3.7a, which are similar for Figure 3.7b also. However, the corresponding reciprocal lattice vectors are marked in Figure 3.7b and the indexing holds well for the diffraction pattern given in Figure 3.7a also. A close look at the diffraction patterns in Figure 3.7a and in Figure 3.7b indicates that essentially there is no difference between them in terms of spot position and their intensities. However, the diffraction spots in Figure 3.7b are more sharply defined than the similar spots in Figure 3.7a. It may be inferred from this observation that there is no phase change that takes places while the quinary oxide is sintered for 10 h and for 100 h. The increase in the sharpness of the spots may be related to the strain relaxation in the lattice that takes place during the long hours of sintering process [24,25]. The d-spacings are marked in Figure 3.7a. Very similar d-spacings were observed in x-ray diffraction patterns for similar samples, which may be indexed to the cubic solid solution phase based on CaO with rocksalt structure with a ~4.78 Å lattice parameter, cubic spinel phase with a ~8.41 Å lattice parameter and a hexagonal phase with a ~2.94 Å and c ~5.28 Å lattice parameter (c/a = 1.8) respectively. It is noted that the hexagonal phase is related to the structural and chemical derivative of the Fe_2O_3 based phase as observed in the x-ray diffraction studies. It is further noted that in this diffraction pattern any signature of the cubic solid solution phase of (CoMgNi)-oxide with rocksalt structure and with a ~4.16 Å lattice parameter could not be observed. It is inferred from this observation that the diffraction pattern is from the Ca and Fe ion rich regions of the sample as observed in the SEM-XEDS chemical maps in Figure 3.4. Now it may be explicitly said that the Ca and Fe rich regions consist of CaO based solid solution phase,

cubic spinel phase and the hexagonal phase. The Co, Mg, Ni rich regions consist of mainly the (CoMgNi)-oxide solid solution phase.

The presence of a large number of spots and their modulation in intensities in Figure 3.7(a-b) can be explained only when the simultaneous presence of all the three phases i. e. the CaO based solid solution phase with rocksalt structure, cubic spinel phase and the hexagonal phase and their oriented growth is taken into consideration. The reciprocal lattice vectors specific to the three different phases, their corresponding d-spacings are marked with different colour scheme in Figure 3.7a. Whereas the zone axis patterns and the indices for three different phases are marked with different colour scheme in Figure 3.7b. In both the figures CaO based cubic solid solution phase with rocksalt structure is marked in green, the cubic spinel phase is marked in yellow and the hexagonal phase, which is supposed to be a structural and chemical derivative of Fe_2O_3 is marked in white. In Figure 3.7b, the zone axis pattern marked in yellow, is the z = $[\bar{1}11]$ pattern from the cubic spinel phase with a ~8.41 Å lattice parameter. In the same figure, the zone axis pattern marked in green corresponds to the z = $[\bar{1}11]$ pattern of the CaO based cubic rocksalt phase with a ~4.78 Å lattice parameter. It is clearly observed that there is an orientation relationship between the CaO based cubic solid solution phase with rocksalt structure and the cubic spinel phase. The orientation relationship is $[\bar{1}11]_{RS} \parallel [\bar{1}11]_S$ and $(220)_{RS} \parallel (2\bar{2}4)_S$ (Rocksalt phase is represented as 'RS' and spinel phase is represented as 'S'). Similarly, the pattern marked in white (Figure 3.7b) is the z = $[2\bar{1}\bar{1}0]$ zone axis pattern of the hexagonal phase with a ~2.94 Å and c ~5.28 Å. This pattern also clearly indicates a strong orientation relationship with the cubic rocksalt phase and the cubic spinel phase.

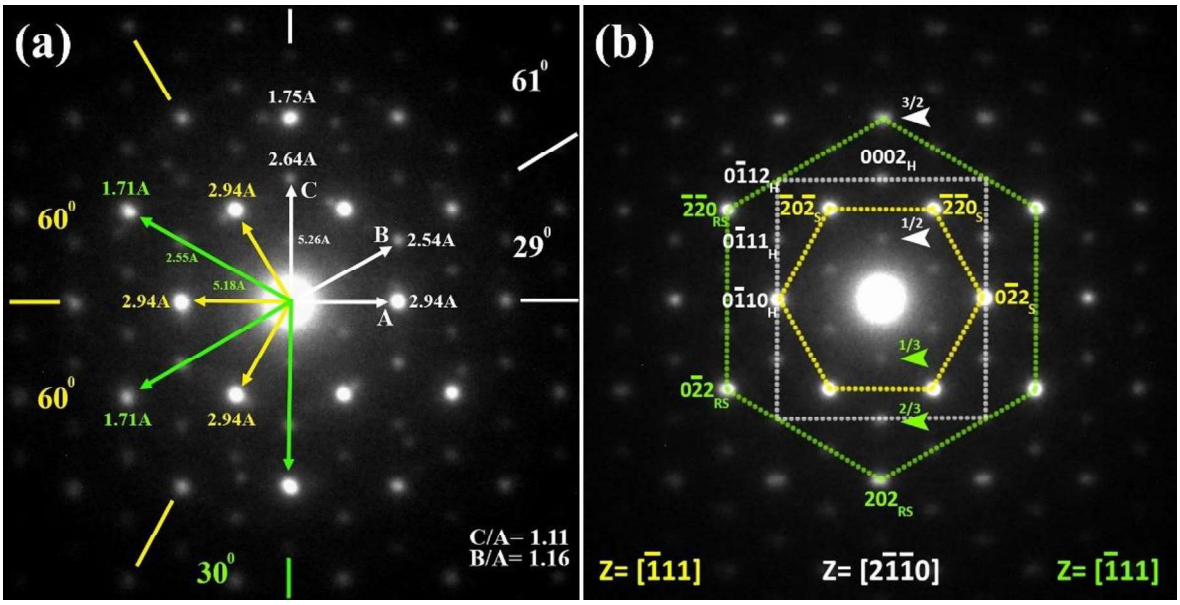

Figure 3.7: Selected area diffraction patterns from the quinary equimolar (CaCoFeMgNi)-oxide after sintering at 1523 K for (a) 10 h (b) 100 h followed by water quenching. In (a) experimentally observed d-spacings and their angular relationships are depicted. In (b) zone axis geometries are depicted. In (a) and (b) the data related to the cubic rocksalt phase, cubic spinel phase and the hexagonal phase are marked in green, yellow and white respectively. The cubic rocksalt phase, cubic spinel phase and hexagonal phase are oriented along z = [$\bar{1}$11], z = [$\bar{1}$11] and z = [2$\bar{1}\bar{1}$0] respectively. Their orientation relationships are [$\bar{1}$11]$_{RS}$ || [$\bar{1}$11]$_S$ and (220)$_{RS}$ || (2$\bar{2}$4)$_S$; [2$\bar{1}\bar{1}$0]$_H$ || [$\bar{1}$11]$_{RS}$ and (0002)$_H$ || ($\bar{2}$02)$_{RS}$; and [2$\bar{1}\bar{1}$0]$_H$ || [$\bar{1}$11]$_S$ and (0002)$_H$ || ($\bar{4}\bar{2}\bar{2}$)$_S$ (RS: Rocksalt, S: Spinel; H: Hexagonal phase).

The orientation relationships are [2$\bar{1}\bar{1}$0]$_H$ || [$\bar{1}$11]$_{RS}$ and (0002)$_H$ || ($\bar{2}$02)$_{RS}$; [2$\bar{1}\bar{1}$0]$_H$ || [$\bar{1}$11]$_S$ and (0002)$_H$ || ($\bar{4}\bar{2}\bar{2}$)$_S$ (Hexagonal phase is represented as 'H'). It is clearly observed that the spots common to any two or more of rocksalt phase, spinel phase or hexagonal phase are more intense than the spots which are unique to either of the three phases. Additionally, ordering induced superlattice reflections are present in Figure 3.7(a-b). The superlattice reflections are marked following the same colour scheme as mentioned earlier (Hexagonal: white, Rocksalt: green). In the hexagonal phase, along 0002 reciprocal lattice vector two superlattice reflections are discerned at ½[0002] and 3/2[0002] (marked with white arrows). Similarly, along the <220> directions of the cubic rocksalt phase, which is also the <0$\bar{1}$11>

direction for the hexagonal phase, superlattice reflections are observed at 1/3<220> and 2/3<220> (marked with green arrows). As the directions are common to both the cubic rocksalt phase and the hexagonal phase, at this moment it cannot be confirmed whether the origin of the superlattice reflections is due to the cubic rocksalt phase or the hexagonal phase. However, in Figure 3.8b, in the zone axis pattern from the hexagonal phase along z = [$2\bar{1}\bar{1}0$] the superlattice reflections are not observed along <$0\bar{1}11$> directions. It can be confirmed from this observation that the additional ordering spots along <220> directions in Figure 3.7(a-b) are due to the cubic rocksalt phase. The physical implications for existence of such superlattice reflections along <0002> directions of the hexagonal phase and <220> directions of the cubic rocksalt phase will be discussed in the discussion section.

TEM bright field images and diffraction patterns from the hexagonal phase reported in the preceding section in the quinary equimolar (CaCoFeMgNi)-oxide after sintering for 10 h and 100 h followed water quenching are given in Figure 3.8(a-c) and Figure 3.8(d-f) respectively. After sintering for 10 h, in the quinary oxide (Figure 3.8a) several parallel fringes (marked with dotted yellow lines) with finite width ~5-10 nm could be observed. The fringes are likely to be originated from a series of planar faults existing within the grain body. The rotationally oriented diffraction pattern (Figure 3.8b) from the same region conforms to the hexagonal phase with a ~2.94 Å and c ~5.28 Å as reported in the preceding section for the same quinary oxide after sintering for 10 h and 100 h (Figure 3.7(a-b)). In the diffraction pattern superlattice reflections at ½[0002] and 3/2[0002] (marked with white arrows) indicating an order along the c-axis of the hexagonal phase is observed. It is to be noted that no superlattice reflection is observed along [$0\bar{1}11$]. Further it is to be noted that the reflections along [$0\bar{1}10$] are not split. However, all other reflections are split into two. It is further observed that a rotation of 180^{o} around 0002 axis leaves the split spots mirror

reflections to one another. This confirms that the parallel fringes in the bright field image in Figure 3.8a are compound deformation twins with shear plane s = $(2\bar{1}\bar{1}0)$, K_1 = (0002), η_1= $[0\bar{1}10]$, K_2 = $[10\bar{1}0]$ and η_2 = $[01\bar{1}1]$ as twin variants. The symbols have their usual meaning in twin crystallography.

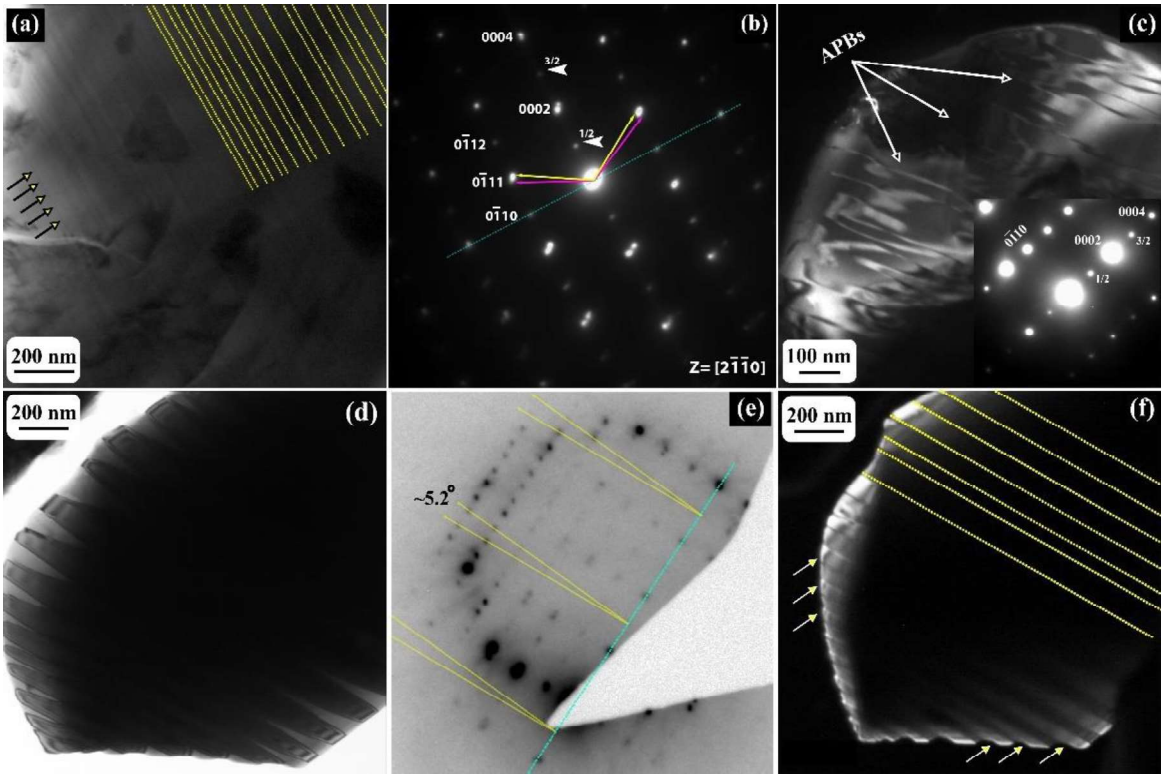

Figure 3.8: TEM (a) BF image and (b) corresponding rotationally aligned selected area diffraction pattern and (c) DF image using the superlattice reflection at ½[0002] (given at the inset in (c)) from the quinary equimolar (CaCoFeMgNi)-oxide after sintering at 1523 K for 10 h followed by water quenching. Linear fringes in (a) are from the twins and the curvilinear contrast in (c) is from the APBs. The diffraction pattern in (b) indicates that the twins in (a) are compound deformation twins with s = $(2\bar{1}\bar{1}0)$, K_1 = (0002), η_1= $[0\bar{1}10]$, K_2 = $[10\bar{1}0]$ and η_2 = $[01\bar{1}1]$ as twin variants. (d) BF image (e) corresponding rotationally aligned diffraction pattern and (f) DF image from the quinary equimolar (CaCoFeMgNi)-oxide after sintering at 1523 K for 100 h followed by water quenching. The diffraction pattern in (e) is little off from the zone axis as shown in (b). All the spots perpendicular to the row of spots marked in cyan are split. The twins in (d) and in (f) are widely spaced.

Dark field image from the same 10 h sintered and quenched sample from a different region in Figure 3.8c and its diffraction pattern at the inset shows that in the dark field image

several curved linear contrasts often resulting into a loop are present. The diffraction pattern in the inset (Figure 3.8c) is along z = $[2\bar{1}\bar{1}0]$. In this diffraction pattern spot splitting is not observed. However, the curvilinear contrast in the image may be correlated with the existence of antiphase domains (antiphase domain boundaries: APBs) within the hexagonal phase (marked with white arrows). The origin of antiphase domains and its physical implications will be discussed in the discussion section.

Similar alternate bright and dark fringe contrast, however, grown to a larger extent is observed in the bright field image (Figure 3.8d) and in the dark field image (Figure 3.8f) of the 100 h sintered and quenched sample (marked with arrows in Figure 3.8f). In the rotationally oriented diffraction pattern (Figure 3.8e) from the same region, which is little away from the nearest zone axis, similar spot splitting is observed. In may be inferred from this observation that the compound deformation twins as shown in the 10 h sintered and quenched sample (Figure 3.8a) grow further in the 100 h quenched sample.

3.4. Discussion

(CaCoFeMgNi)-oxide was synthesized through solid state route, in which the green compact was sintered at 1523 K for different lengths of time and they were water quenched. Lower order derivatives of the quinary equimolar oxide i.e. (CoMgNi)-oxide, (CaCoMgNi)-oxide were also synthesized and they were subjected to similar processing conditions in order to compare the phase evolution, microstructural stability against a standard set of conditions. The effect of processing route also has been investigated. A unified look at the results leads to some fundamental understanding about this multicomponent oxide, its phase and structure evolution, their oriented intergrowth, distribution of chemistry and microstructural stability, which will be discussed in the subsequent sections. At the end, an attempt will be made to comment whether entropy is

the only determining factor or there is an interplay of several other factors that ultimately decide its phase, microstructure evolution, its stability and hence, its properties.

3.4.1. Phase and microstructure evolution and its stability

The precursor oxides leading to the formation of quinary equimolar (CaCoFeMgNi)-oxide are CaO, CoO, FeO, MgO and NiO. All the individual oxides are having cubic rocksalt structure [24-25]. CoO, FeO and NiO may exist in other crystal structures as they can exist in several oxidation states and they can switch their oxidation states quite easily [26]. Cubic spinel variant of Co_3O_4 and Fe_3O_4 has also been reported. Fe_2O_3 is the hexagonal/rhombohedral variant that is quite abundantly available in nature. However, there is a structural correlation between the cubic rocksalt phase and the spinel phase. In the cubic rocksalt phase, all the octahedral voids are filled with cations whereas in cubic spinel half of the octahedral voids are filled with cations. In case of hexagonal Fe_2O_3 2/3rd of the available octahedral voids are filled with cations. Their structural relationship will be discussed in detail in the subsequent sections.

It has been widely reported in literature that systematic replacement of ions for a ceramic crystal or atoms for a metallic crystal may lead to the formation of single phase multicomponent solid solution/intermetallic/compound-based materials [20, 22-23, 27-28]. However, systematic replacement should be such that the multicomponent materials become equimolar or almost equimolar. In the present work, all the precursor oxides with cubic rocksalt structure were put together in equimolar proportions with an expectation that they will form single phase solid solution through systematic replacement. Contrary to the expectation, it has been observed that ternary equimolar (CoMgNi)-oxide formed single phase solid solution after sintering and quenching, where under similar processing condition quaternary equimolar (CaCoMgNi)-oxide formed two cubic solid solution phases with rocksalt structure and with two different lattice parameters. One of the solid solution

phases is based on CaO and other one is based on (CoMgNi)-oxide. It may be inferred that Ca^{2+} cations were not completely accepted in the isostructural lattice of the solid solution phase of (CoMgNi)-oxide. Upon addition of Fe^{2+}/Fe^{3+} ions, additional phases with rhombohedral/hexagonal structure and cubic spinel phase are also observed. The cation radii of Ca^{2+}, Co^{2+}, Mg^{2+}, Ni^{2+} and Fe^{2+} are ~ 1 Å, 0.75 Å, 0.72 Å, 0.69 Å and 0.78 Å respectively [24-25]. The cation radii are reported based on their 6-fold coordination environment. It is evident from the cation radii that except for Ca^{2+}, all other cation radii are within ~12% difference. Equimolar addition of CoO with MgO or NiO leads to the partial replacement of cations in the crystal lattice with rocksalt structure and their cation radii being close to one another introduction of micro strain in the lattice is not enough to frustrate and destabilise the original crystal lattice. However, upon addition of CaO, due to the large difference in cation radii of Ca^{2+} ion with the remaining ions, the original rocksalt lattice is strained and it rejects most of the Ca^{2+} ions leading to the formation of another solid solution phase with rocksalt structure but with different lattice parameter. Introduction of lattice strain to frustrate/destabilise a crystal has been reported in metallic systems also and its manifestation in other extreme is the formation of metallic glasses [29-31]. In multicomponent or high entropy materials even though single-phase solid solution or compounds with five or more elements have been reported, their stability is still under investigation due to the presence of strain apart from other thermodynamic factors. It has been reported in multicomponent metallic alloys that composition migration takes place upon ageing [32]. In CoFeGaMnZn multicomponent oxide compositional phase separation has been reported leading to the formation of chessboard-like microstructure [33-34]. The compositional segregation is quite evident in the present study also. As observed from the SEM-XEDS maps (Figure 3.4), in the quinary (CaCoFeMgNi)-oxide, two distinct regions one rich in Ca and Fe ions and other rich in Co, Mg and Ni ions are present. Two different

solid solution phases with rocksalt structures but with different lattice parameters are observed in two compositionally segregated regions. In the Ca and Fe ion rich regions additional ordered hexagonal/rhombohedral phase and spinel phase are observed.

A quick look at the binary phase diagrams of different binary combinations of the quinary oxide under study reveals that many of the phase diagrams are isomorphous, quite a few of them show solid solutioning along with binary invariant reactions. None of them show any immiscibility. However, in the quinary oxide clear composition segregation is observed. This clearly indicates that ternary, quaternary and quinary interactions should also be taken into account in order to predict phase formation and its stability in multicomponent oxides. It has been reported in earlier literature that similar cation radii at a specific oxidation state and coordination environment, presence of immiscibility in at least one pair of components and non-isostructuralism in at least one component are the essential criteria for the formation of single-phase solid solution in multicomponent materials [14, 23]. The quinary oxide studied in the present work does not meet any of the criteria. However, the experimental validation of the postulates should be investigated further. It has also been reported that isostructuralism [23] would anyway promote the formation of single-phase solid solution which is proved to be not valid for the quinary oxide studied in the present work.

3.4.2. Strain minimization and oriented intergrowth of phases

Quinary (CaCoFeMgNi)-oxide upon sintering and quenching forms two chemically segregated regions comprising of mainly two solid solution phases with rocksalt structure along with a spinel phase and an ordered hexagonal phase. The electron diffraction patterns from the same solid solution phase after 10 h of sintering at 1523 K followed by quenching shows well defined diffraction spots (Figure 3.6(a-d)). However, in the bright field image mottled contrast typical of accumulated strain fields are observed. The structure of the same

phase remains to be cubic rocksalt with similar lattice parameter after sintering for 100 h followed by quenching. However, in the electron diffraction patterns and in the bright field images some new features are observed (Figure 3.6 (e-h)). In the diffraction patterns the spots are transformed into arcs with modulation of intensities and in the bright field images fringe contrast (marked by arrows) is observed. When the modulated intensity maxima in the diffraction patterns are connected geometrically, several symmetry shapes corresponding to the cubic zone axis, however, rotated with respect to one another are observed. It clearly indicates that there are domains with cubic crystal structures, which are rotated with respect to one another through a very small angle. The presence of arcs in both the diffraction patterns (Figure 3.6f and Figure 3.6h) confirms that the cubic domains are having in-plane and out-of-plane rotation with respect to one another. A schematic diagram of such rotated cubic domains in 3D is given in Figure 3.9a. It is inferred from the diffraction patterns and from the schematic diagram that during long time sintering, in the cubic solid solution phase of (CoMgNi)-oxide, cubic domains are formed and they are rotated with respect to one another. This observation pertains to the tendency of the solid solution phase to minimize it lattice and interface strain during the long-time sintering. During long-time sintering, in the original solid solution phase of (CoMgNi)-oxide composition modulation develops that helps in reducing the lattice strain by preferentially enriching one domain by one kind of ion. However, in this process, lattice parameter of each domain also changes, even though negligibly. The local change in lattice parameter manifests itself as interfacial strain between different domains. In order to minimize the interfacial strain, the compositionally modulated domains rotate with respect to one another. Each of the compositionally modulated domains are represented by different colours in the schematic diagram in Figure 3.9a. Their rotation in order to reduce the interfacial strain is also observed in the schematic.

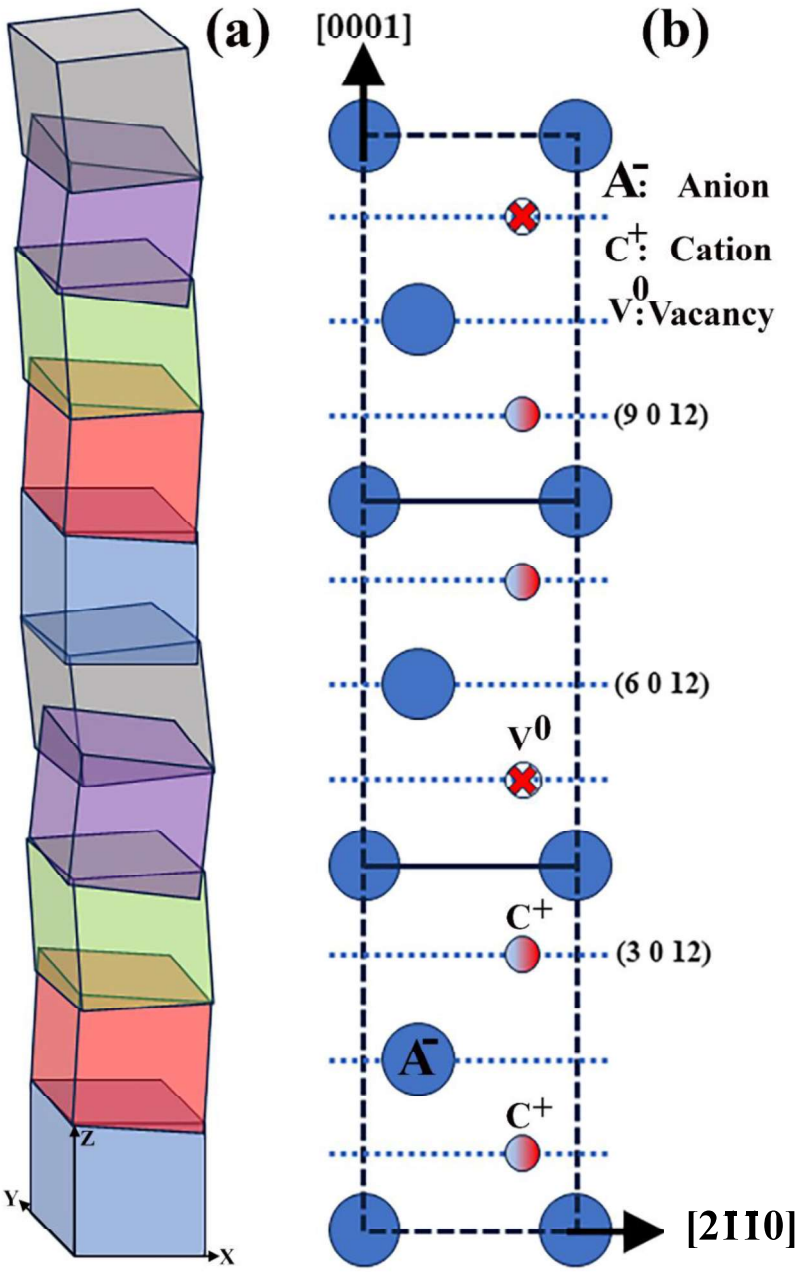

Figure 3.9: (a) Schematic representation of the mutually rotated domains in the intergrown helical arrangement with cubic rocksalt structure stacked along [001] direction. Possible composition modulation in each domain is marked with different colours. (b) [2$\bar{1}\bar{1}$0] orthographic projection of the hexagonal phase with 2/3rd octahedral voids filled up. Cation ordering with vacancies along [0001] is depicted.

Presence of such domains leads to the formation of fringe contrast within the mottled regions in the bright field images (marked with arrows, Figure 3.6e and Figure 3.6g). The width of the fringes may be directly correlated with the size of the compositionally

modulated domains. It has been reported theoretically that such kind of helical structures may form in oxides [35-36]. However, experimental evidence of such rotated helical structures in multicomponent oxide has not been reported before. In the Ca and Fe ion rich regions of the quinary oxide, after sintering at 1523 K for different lengths of time followed by quenching, solid solution phase with cubic rocksalt structure with ~4.78 Å lattice parameter, a spinel phase with ~8.41 Å lattice parameter and a hexagonal phase with a ~2.94 Å, c ~5.28 Å lattice parameter are observed. It is evident from the electron diffraction patterns from these phases after 10 h and 100 h of sintering that the phases grow with a very strong orientation relationship (Figure 3.7a-b). After 10 h of sintering, the diffraction spots (Figure 3.7a) are relatively smeared out, whereas the same diffraction spots become quite sharply defined after 100 h of sintering (Figure 3.7b). This observation clearly indicates that there is no change in orientation relationship among the phases, however, enhancement in sharpness of the diffraction spots may be related to the reduction in strain in the phases. Several orientationally related phases may be indexed from the diffraction patterns (Figure 3.7a-b). They are marked with different colours. The d-spacings are marked in Figure 6a and corresponding reciprocal vectors are marked in Figure 3.7b. From the z = $[2\bar{1}\bar{1}0]$ zone axis pattern of the hexagonal phase, superlattice reflections at 1/2[0002] and 3/2[0002] are observed. This clearly indicates ordering in the hexagonal phase along [0002] and the positions of the superlattice reflections ascertains that the original hexagonal lattice is tripled along [0002] direction due to ordering. The orthographic projection of the hexagonal lattice along $[2\bar{1}\bar{1}0]$ direction is given in Figure 3.9b. It is observed that 2/3rd of the octahedral voids are filled with cations and there is an ordering between the cations and the vacancies, which leads to the origination of the superlattice reflections at 1/2[0002] and 3/2[0002]. Partial occupancy of the tetrahedral voids will also lead to ordering, however, in that case the position of the superlattice reflections will be different. Cation and vacancy

ordering along [0002] direction also makes sure maximum possible separation between the cations, which in turn reduces the energy of the crystal. Development of this order in this crystal may be seen as an attempt by the crystal to reduce its energy by maximizing the separation between the similarly charged cations.

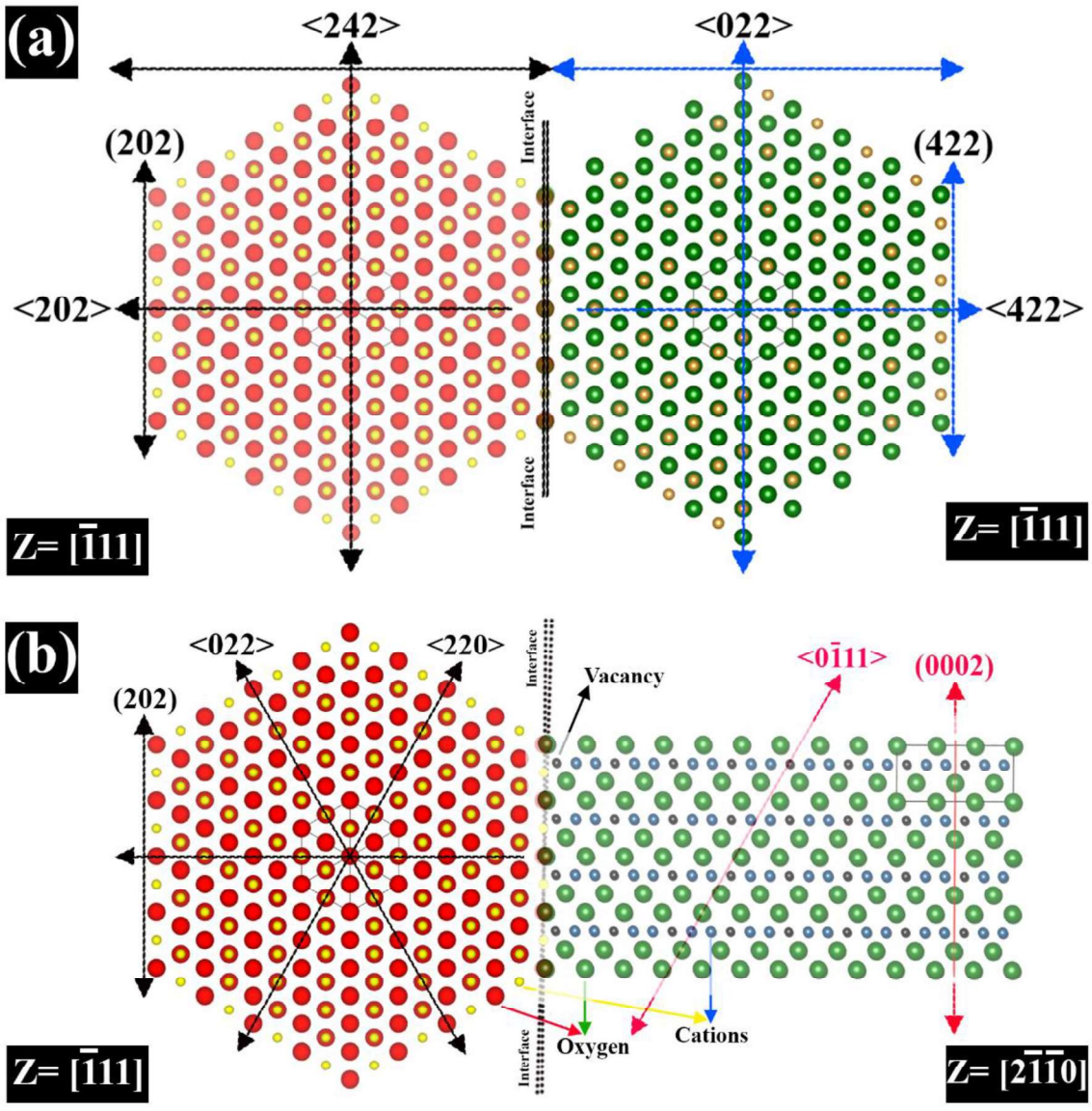

Figure 3.10: (a) Schematic (202) || (422) interface between cubic rocksalt and cubic spinel phase. The interface is coherent. (b) schematic representation of (202) || (0002) interface between the cubic rocksalt phase with the hexagonal phase. The interface in semicoherent with quite minimal incoherency strain. The schematic diagrams are developed from the experimentally observed orientation relationships and the calculated crystallographic data from the diffraction patterns.

It is worth mentioning that existence of such charged cation pairs separated by vacancies may lead to the formation of dipoles [25], which may originate novel properties in such crystals with several cations in the lattice. It is also to be noted that a hexagonal/rhombohedral phase was identified from the x-ray diffraction pattern of this sample (Figure 3.1-5C), which was pointed out to be correlated with hexagonal/rhombohedral Fe_2O_3 phase. It is now evident that the hexagonal phase obtained in the Ca and Fe ion rich regions is indeed a chemical and structural derivative of hexagonal/rhombohedral Fe_2O_3 phase. In both the diffraction patterns in Figure 3.7(a-b), a strong orientation relationship is observed between the cubic solid solution phase with rocksalt structure, cubic spinel phase and the hexagonal phase. In the cubic solid solution phase with rocksalt structure, superlattice reflections at 1/3[220] and 2/3[220] reciprocal lattice vectors are observed. It necessarily means that ordering takes place along <220> directions of the rocksalt phase that triplicates the cubic lattice. The orthographic projection of the solid solution phase with rocksalt structure (Figure 3.10a) along [111] shows that cation order takes place along <220> directions. The cubic spinel phase is oriented with the rocksalt phase such that $[\bar{1}11]_{RS} \parallel [\bar{1}11]_S$ and $(220)_{RS} \parallel (2\bar{2}4)_S$ (Rocksalt phase is represented as 'RS' and spinel phase is represented as 'S'), which necessarily means that the spinel phase is having 30^o in-plane rotation with respect to the rocksalt phase. However, ordering in the spinel phase could not be ascertained. The interface diagram for the cubic rocksalt phase and the spinel phase is shown in Figure 3.10a. The interface is absolutely coherent. This orientation relationship develops in order to minimize the strain energy of the interface. Similar coherent interfaces have been observed between rocksalt and spinel phases before. It is worth mentioning that rocksalt phase might undergo rhombohedral distortion and still may remain coherent with the spinel phase. In the present study, no definite proof for rhombohedral distortion of the rocksalt phase has been observed [37].

Similar orientation relationship is observed between the cubic rocksalt phase and the hexagonal phase. As stated before, the orientation relationship is $[2\bar{1}\bar{1}0]_H \parallel [\bar{1}11]_{RS}$ and $(0002)_H \parallel (\bar{2}0\bar{2})_{RS}$; $[2\bar{1}\bar{1}0]_H \parallel [\bar{1}11]_S$ and $(0002)_H \parallel (\bar{4}\bar{2}\bar{2})_S$ (Hexagonal phase is represented as 'H'). From the interface diagram (Figure 3.10b), it is evident that the interface between cubic rocksalt and the hexagonal phase is semi-coherent. Here again, the tendency of the system to reduce its interface energy is quite evident that leads to oriented intergrowth. Similar, orientation relationship is observed between the cubic spinel phase and the hexagonal phase. The orientation relationship has been stated before. The interface structure is quite similar to the interface between cubic rocksalt phase and the hexagonal phase. It is semi-coherent in nature. In this interface structure also, the tendency of system to reduce its interface energy is strongly evident.

3.4.3. Free energy stabilization through internal energy, strain energy and configurational entropy

Energetics, enthalpy and configurational entropy of multicomponent materials has been discussed since the discovery of metastable materials [38-39]. During rapid solidification or mechanical alloying, formation of metastable phases, extension of solid solubility, bulk metallic glasses (BMGs) or bulk amorphous alloys (BAAs) etc. were reported several decades back [30-31]. Even though BMGs are multicomponent in nature, they are most often not equimolar. They may be treated as dilute multicomponent alloys. Since the discovery of BMGs, the science of glass formation and its alloy design strategies have mostly progressed through empiricism. Presence of more than three elements with widely different atomic sizes frustrates the crystal lattice due to the introduction of unusually large amount of micro-strain in the lattice, that ultimately leads to the glass formation. The structural frustration of the crystal lattice due to presence of micro-strain may be considered as inverse Hume-Rothery rule of solid solution formation. High negative enthalpy of

mixing among the constituent elements favours glass formation. It is famously known as Inoue's criteria of BMG formation. BMG forming alloys discovered so far mostly can be explained in the light of Inoue's criteria of BMG formation.

Multicomponent high entropy alloys (HEAs), which are of recent vintage, have also been dealt with empiricism [10-11]. Presence of multiple elemental species in the same crystal lattice increases the configurational entropy of the system so high that the HEAs are always stabilized by entropy. However, over last two decades, high entropy intermetallic phases have also been reported [27-28], where existence of order essentially will not allow the configurational entropy to be as high as a high entropy solid solution phase. Additionally, many of the HEAs have shown metastability in the temperature-composition space, which necessarily makes the high entropy stabilization concept questionable [32]. Currently it is also believed that the term HEA is a misnomer, rather it should be termed as multi-principal element alloys (MPEAs) or complex concentrated alloys (CCAs) [9, 20].

High entropy oxides (HEOs) or high entropy ceramics (HECs) is of latest vintage and in these materials, the configurational entropy is calculated separately for the cation and anion sublattice before they are added together in order to assess the total entropy [18, 22]. In HEOs/HECs also order may exist, which will not allow the configurational entropy to be as high as a random multicomponent solid solution. However, the stabilization of HEOs/HECs is believed to be entropy driven, i. e. the total entropy of the cation and anion sublattice is so high that the free energy of the phase is always dominated by the high negative value of TS (T: Temperature, S: configurational entropy) term. This has given birth to the term entropy stabilized materials (ESMs) for this class of oxides or ceramics [40]. In the present study, a strong and well-defined tendency of the system to minimize its strain energy has been observed. Ternary (CoMgNi)-oxide, after sintering leads to the formation of single solid solution phase with rocksalt structure. However, upon addition of CaO, the

quaternary (CaCoMgNi)-oxide, after sintering forms two solid solution phases with rocksalt structure, however, with two different lattice parameters. This observation may be explained in the light of their difference in atomic radii, introduction of micro-strain in the lattice and the tendency of the system to reduce its micro-strain further by compositionally separating into two different phases. In quinary equimolar (CaCoFeMgNi)-oxide, after sintering, two compositionally segregated regions are observed in the microstructure. In addition to that, compositionally modulated domains with in-plane and out-of-plane rotation, leading to a helical structure is observed after long time sintering in the (CoMgNi)-oxide solid solution phase. In the Ca and Fe ions rich regions, oriented intergrowth of the solid solution phase, spinel phase and the hexagonal phase is observed. The interface diagram of the three inter grown phases with strong orientation relationship shows that the interfaces are coherent or semi-coherent in nature. In addition, APBs in the hexagonal phase further points towards the tendency of the system to minimize its strain energy, often at the cost of a finite reduction in configurational entropy.

Free energy change (ΔG) may be represented as $\Delta G = \Delta H - T\Delta S$ at constant temperature and pressure, where the symbols have their usual meaning. Again, $\Delta H = \Delta U + P\Delta V$, where $P\Delta V$ represents mechanical energy involved in the process. In condense matter systems, the numerical value of $P\Delta V$ at constant P will not be very high. However, it relates to the strain energy and its physical manifestations are micro strain in the lattice, around the defects and interfaces. The expression of free energy may be written as $\Delta G = \Delta U + P\Delta V - T\Delta S$. Configurational entropy (ΔS) being always positive, the term $T\Delta S$ is always positive. The mechanical energy term $P\Delta V$ is always positive. The internal energy (ΔU) is an intrinsic property of the system. Now the trade-off between the mechanical strain energy $P\Delta V$ and the entropy term $T\Delta S$ will determine the stability of a system in the free energy landscape. In case of the multicomponent (CaCoFeMgNi)-oxide single solid solution phase

formation would definitely increase the configurational entropy, however, the positive contribution from the strain energy component would nullify the energetic advantage in the free energy landscape. So, the multicomponent oxide compositionally segregates in order to strike a trade-off between entropy and strain energy. Further, oriented growth of solid solution phase, spinel phase and hexagonal phase with coherent and semi-coherent interfaces reduces the positive contribution of the strain energy in order to achieve further advantage in the free energy landscape. The formation of compositionally modulated helical structures in the (CoMgNi)-oxide solid solution phase after long time sintering proves that within the helical structures the distribution of the cations is still macroscopically random, hence configurational entropy remains high. However, compositional modulation and the relative rotation among the domains reduces the strain energy. Through this arrangement, the system is able to maximize the negative contribution of the entropy term, however, in turn it reduces the positive contribution of the strain energy term. Thus, it is able to maximize its energetic advantage in terms of free energy. It is clearly seen that the stability of this multicomponent oxide is a trade-off between entropy and strain energy. Widely believed entropy stabilization in this class of materials should be thoroughly reinvestigated in the light of the possible trade-off between entropy and strain energy. It should be noted that in this qualitative explanation only configurational entropy has been considered, other entropy contribution should also be taken into account in order to arrive at a more accurate analysis of the stability of phases in this class of materials.

3.5. Conclusions

I. Two chemically segregated regions; one enriched in Ca and Fe ions and another in Co, Mg, Ni ions is produced in the microstructure of quinary equimolar multicomponent (CaCoFeMgNi)-oxide upon sintering at 1523 K for different lengths of time followed by water quenching. In the Co, Mg, Ni rich region ternary

solid solution of (CoMgNi)-oxide with cubic rocksalt structure with ~4.21 Å lattice parameter is observed. In the Ca, Fe ion rich regions, three phases namely; CaO based solid solution phase with cubic rocksalt structure with ~4.78 Å lattice parameter, a cubic spinel phase with ~8.41 Å lattice parameter and a hexagonal phase with a = 2.94 Å and c = 5.28 Å lattice parameter are observed. Ordering of cations and vacancy takes place in the octahedral voids of the hexagonal phase.

II. Ternary (CoMgNi)-oxide and quaternary (CaCoMgNi)-oxide, derivative of the original quinary equimolar multicomponent (CaCoFeMgNi)-oxide, after sintering at 1523 K for different lengths of time followed by quenching produces the same solid solution phases with cubic rocksalt structure as obtained in the quinary equimolar oxide. Intermediate mechanical alloying before sintering does not alter the phase and microstructure evolution in the quinary and its ternary and quaternary derivative oxides.

III. In the (CoMgNi)-oxide solid solution phase after sintering the quinary oxide for 100 h at 1523 K followed by quenching, mutually rotated cubic domains with rocksalt structure is observed. Chemical modulation and mutual rotation among the domains leading to helical structure is likely to reduce lattice and interface strain arising out of different cation radii and incoherency at the interfaces.

IV. In the Ca and Fe ion rich regions in the quinary oxide, after sintering at 1523 K for different lengths of time, highly oriented growth of the solid solution phase with rocksalt structure, cubic spinel phase and hexagonal phase is observed. The interfaces of these phases are either coherent or semi-coherent. It is due to the tendency of the quinary oxide to reduce its strain energy of the interfaces.

V. The orientation relationship of the cubic solid solution phase with rocksalt structure with the cubic spinel phase and with the hexagonal phase are $[\bar{1}11]_{RS} \parallel [\bar{1}11]_S$ and $(220)_{RS} \parallel (2\bar{2}4)_S$; $[2\bar{1}\bar{1}0]_H \parallel [\bar{1}11]_{RS}$ and $(0002)_H \parallel (\bar{2}0\bar{2})_{RS}$; and $[2\bar{1}\bar{1}0]_H \parallel [\bar{1}11]_S$ and $(0002)_H \parallel (\bar{4}\bar{2}\bar{2})_S$ (RS: Rocksalt, S: Spinel; H: Hexagonal phase).

VI. Extensive compound deformation twins with $s = (2\bar{1}\bar{1}0)$, $K_1 = (0002)$, $\eta_1 = [0\bar{1}10]$, $K_2 = [10\bar{1}0]$ and $\eta_2 = [01\bar{1}1]$ as twin variants are observed along with anti-phase boundaries (APBs) in the hexagonal phase. Ordering and twinning in the hexagonal phase takes place in a bid to relax its lattice strain.

VII. Configurational entropy is not the sole stabilizing factor in the quinary oxide. It is a trade-off between the configurational entropy and the strain energy that stabilises the phases by minimizing its free energy.

3.6. Reference

1. Z. Lun, B. Ouyang, D. H. Kwon, Y. Ha, E. E. Foley, T. Y. Huang, Z. Cai, H. Kim, M. Balasubramanian, Y. Sun, J. Huang, Y. Tian, H. Kim, B. D. McCloskey, W. Yang, R. J. Clement, H. Ji, G. Ceder, Cation-disordered rocksalt-type high-entropy cathodes for Li-ion batteries, Nature Mater., 2021, Vol. 20, 214-221.
2. A. Sarkar, Q. Wang, A. Schiele, M. R. Chellali, S. S. Bhattacharya, D. Wang, T. Brezesinski, H. Hahn, L. Velasco, B. Breitung, High-entropy oxides: fundamental aspects and electrochemical properties, Adv. Mater., 2019, 1806236 (9 pages).
3. C. Oses, C. Toher, S. Curtarolo, High-entropy ceramics, Nature Rev. Mater., 2020, Vol. 5, 295-309.

4. Y. Gu, A. Bao, X. Wang, Y. Chen, L. Dong, X. Liu, H. Pan, Y. Li, X. Qi, Engineering the oxygen vacancies of rocksalt-type high-entropy oxides for enhanced electrocatalysis, Nanoscale, 2022, Vol. 14, 515-524.
5. M. P. Jimenez-Segura, T. Takayama, D. Berardan, A. Hoser, M. Reehuis, H. Takagi, N. Dragoe, Long-range magnetic ordering in rocksalt-type high-entropy oxide, Appl. Phys. Lett., 2019, Vol. 114, 122401 (5 pages).
6. B. L. Musico, D. Gilbert, T. Z. Ward, K. Page, E. George, J. Yan, D. Mandrus, V. Keppens, The emergent field of high entropy oxides: design, prospect, challenges and opportunities for tailoring material properties, APL Mater., 2020, Vol. 8, 040912 (16 pages)
7. H. Jia, M. Horton, Y. Wang, S. Zhang, K. A. Persson, S. Meng, M. Liu, Persona of transition metal ions in solids: a statistical learning on local structures of transition metal oxides, Adv. Sci., 2022, 220756 (9 pages).
8. D. Berardan, S. Franger, A. K. Meena, N. Dragoe, Room temperature lithium superionic conductivity in high entropy oxide, J. Mater. Chem. A, 2016, Vol. 4, 9536-9541.
9. W. Steurer, Single-phase high entropy alloys: a critical update, Mater. Char., 2020, Vol. 162, 110179 (17 pages).
10. B. Cantor, I. T. H. Chang, P. Knight, A. J. B. Vincent, Microstructural development in equiatomic multicomponent alloys, Mater. Sci. Eng. A, 2004, Vol. 375-377, 213-218.
11. J. W. Yeh, S. K. Chen, S. J. Lin, J. Y. Gan, T. S. Chin, T. T. Shun, C. H. Tsau, S. Y. Chang, Nanostructured high-entropy alloys with multiple principal elements: novel alloy design concepts and outcomes, Adv. Eng. Mater., 2004, Vol. 6 (5), 299-303.

12. K. C. Pitike, K. C. Santosh, M. Eisenbach, C. A. Bridges, V. R. Cooper, Predicting the phase stability of multicomponent high-entropy compounds, Chem. Mater., 2020, Vol. 32, 7507-7515.
13. M. Fracchia, M. Coduri, M. Manzoli, P. Ghigna, U. A. Tamburini, Is configurational entropy the main stabilizing term in rock-salt $Mg_{0.2}Co_{0.2}Ni_{0.2}Cu_{0.2}Zn_{0.2}O$ high entropy oxide?, Nature Comm., 2022, Vol. 13, 2977 (4 pages).
14. C. M. Rost, E. Sachet, T. Borman, A. Moballegh, E. C. Dickey, D. Hou, J. L. Jones, S. Curtarolo, J. P. Maria, Entropy-stabilized oxide, Nature Comm., 2015, Vol. 6, 8485 (8 pages).
15. Y. Zhang, T. T. Zuo, Z. Tang, M. C. Gao. K. A. Dahmen, P.K.Liaw, Z. P. Lu, Microstructure and properties of high-entropy alloys, Prog. Mater. Sci., 2014, Vol. 61, 1-93.
16. G. Anand, A. P. Wynn, C. M. Handley, C. L. Freeman, Phase stability and distortion in high entropy oxides, Acta Mater., 2018, Vol. 146, 119-125.
17. D. Ma, B. Grabowski, F. Kormann, J. Neugebauer, D. Raabe, *Ab initio* thermodynamics of CoCrFeMnNi high entropy alloy: importance of entropy contributions beyond the configurational one, Acta Mater., 2015, Vol. 100, 90-97.
18. S. J. McCormack, A. Navrotsky, Thermodynamics of high entropy oxides, Acta Mater. 2021, Vol. 202, 1-21.
19. O. N. Senkov, J. D. Miller, D. B. Miracle, C. Woodward, Accelerated exploration of multi-principal element alloys with solid solution phases, Nature Comm., 2015, Vol. 6, 6529 (10 pages).
20. D. B. Miracle, O. N. Senkov, A critical review of high entropy alloys and related concepts, Acta Mater., 2017, Vol. 122, 448-511.

21. D. Berardan, A. K. Meena, S. Franger, C. Herrero, N. Dragoe, Controlled Jahn-Teller distortion in (MgCoNiCuZn)O-based high entropy oxides, J. Alloys Comp., 2017, Vol. 7, 693-700.
22. C. M. Rost, Z. Rak, D. W. Brenner, J. P. Maria, Local structure of the $Mg_xNi_xCo_xCu_xZn_xO$ (x = 0.2) entropy stabilized oxide: EXAFS study, J. Am. Ceram. Soc., 2017, Vol. 00, 1-7.
23. A. Sarkar, R. Djenadic, N. J. Usharani, K. P. Sanghvi, V. S. K. Chakravadhanula, A. S. Gandhi, H. Hahn, S. S. Bhattacharya, Nanocrystalline multicomponent entropy stabilized transition metal oxides, J. Eu. Ceram. Soc., 2017, Vol. 37, 747-754.
24. C. B. Carter, M. G. Norton, Ceramic Materials Science and Engineering, Spinger, 2nd Edition, New York 2013
25. Y. M. Chiang, D. P. Birnie, W. D. Kingery, Physical Ceramics: principles for ceramic science and engineering, Wiley Publication, 1997, USA.
26. J. Basu, R. Divakar, In-situ electron microscopy investigation of reduction-induced microstructural changes in NiO, Ceram. International, 2015, Vol. 41(10), 12658-12667.
27. N. Zhou, S. Jiang, T. Huang, M. Qin, T. Hu, J. Luo, Single-phase high-entropy intermetallic compounds (HEICs): bridging high-entropy alloys and ceramics, Sci. Bulletin, 2019, Vol. 64, 856-864.
28. T. H. Chou, J. C. Huang, C. H. Yang, S. K. Lin, T. G. Nieh, Consideration of kinetics on intermetallics formation in solid-solution high entropy alloys, Acta Mater., 2020, Vol. 195, 71-80.
29. J. Basu, S. Ranganathan, Glass-forming ability and stability of ternary Ni-early transition metal (Ti/Zr/Hf) alloys, Acta Mater. 2008, Vol. 56, 1899-1907.

30. A. Inoue, Stabilization of metallic supercooled liquid and bulk amorphous alloys, Acta Mater., 2000, Vol. 48, 279-306.
31. J. Basu, S. Ranganathan, Bulk metallic glasses: a new class of engineering materials, Sadhana, 2003, Vol. 28, 783-798.
32. V. Shivam, J. Basu, R. Manna, N. K. Mukhopadhyay, Local composition migration induced microstructural evolution and mechanical properties of non-equiatomic $Fe_{40}Cr_{25}Ni_{15}Al_{15}Co_5$ medium entropy alloy, Met. Mater. Trans. A, 2021, Vol. 52, 1777-1789.
33. A. S. Pal, A. K. L. Das, A. Singh, K. M. Knowles, Md. I. Ahmad, J. Basu, Evolution of self-assembled chessboard nanostructure spinel in a CoFeGaMnZn multicomponent oxide, Philos. Mag., 2022, Vol. 102(12), 1121-1135.
34. A. S. Pal, A. K. L. Das, K. Gururaj, M. Sadhasivam, K. M. Knowles, Md. I. Ahmad, K. G. Pradeep, J. Basu, Nanoarchitectonics of self-assembled chessboard-like structures by recurrent phase separation and coalescence of nano domains in CoFeMn oxide, Acta Mater., 2023, Vol. 242, 118423 (12 pages).
35. V. M. Talanov, V. B. Shirokov, Tilting structures in spinels, Acta Cryst., 2012, Vol. A68, 595-606.
36. B. G. Hyde, A. N. Bagshaw, S. Andersson, M. O'Keeffe, Some defect structures in crystalline solids, Annu. Rev. Mater. Sci., 1974, Vol. 4, 43-92.
37. A. Singh, S. Yasui, A. S. Pal, L. A. Bendersky, I. Takeuchi, R. K. Mandal, J. Basu, Structure and interfaces of compositionally graded $Li(Ni, Mn)_xO_y$ cathodes on (111) Nb-doped $SrTiO_3$, Philos. Mag., 2022, Vol. 102(16), 1547-1579.
38. P. Duwez, Metastable phases obtained by rapid quenching from the liquid state, Prog. Solid State Chem., 1967, Vol. 3, 377-400.

39. B. S. Murty, S. Ranganathan, Novel materials synthesis by mechanical alloying/milling, Int. Mater. Rev., 1998, Vol. 43, 101-141.
40. M. Brahlek, M. Gazda, V. Keppens, A. R. Mazza, S. J. McCormack, A. M. Gryn, B. Musico, K. Page, C. M. Rost, S. B. Sinnott, C. Toher, T. Z. Ward, A. Yamamoto, What is in a name: defining “high entropy” oxides, APL Mater. 2022, Vol. 10, 110902 (12 pages).